

Magnetism on the stretched $\mathcal{H}\langle-1\rangle$ harmonic honeycomb in lanthanide orthotantalates

Nicola D. Kelly,^{1,*} Lei Yuan,¹ Rosalyn L. Pearson,^{1,†} Emmanuelle Suard,² Inés Puente Orench,^{2,3} and Siân E. Dutton^{1,‡}

¹*Cavendish Laboratory, University of Cambridge,
J J Thomson Avenue, Cambridge, CB3 0HE, UK*

²*Institut Laue-Langevin, 71 Avenue des Martyrs, 38000 Grenoble, France*

³*Instituto de Nanociencia y Materiales de Aragón (INMA),
CSIC-Universidad de Zaragoza, Zaragoza, 50009, Spain*

(Dated: March 4, 2022)

The magnetic Ln^{3+} ions in the fergusonite and scheelite crystal structures form a truncated hyperhoneycomb net that can be labelled as $\mathcal{H}\langle-1\rangle$ by analogy with the harmonic honeycomb series $\mathcal{H}\langle N\rangle$ [Modic *et al.*, *Nat. Commun.* **5**, 4203 (2014)]. This $\mathcal{H}\langle-1\rangle$ magnetic lattice is an elongated form of the diamond lattice and is therefore predicted to host exotic magnetic ground states. In this study, polycrystalline samples of the fergusonite orthotantalates M - $LnTaO_4$ ($Ln = Nd, Sm, Eu, Gd, Tb, Dy, Ho, Er$) are synthesized and then characterized using powder diffraction and bulk magnetometry and heat capacity. $TbTaO_4$ orders antiferromagnetically at 2.25 K into a commensurate magnetic cell with $\vec{k} = 0$, magnetic space group $14.77 (P2_1'/c)$ and Tb moments parallel to the a -axis. No magnetic order was observed in the other materials studied, leaving open the possibility of exotic magnetic states at $T < 2$ K.

I. INTRODUCTION

Magnetism on diamond-like lattices has been widely studied in both coordination frameworks [1] and ceramic systems, including materials with the scheelite crystal structure such as $KRuO_4$ [2] and $KOsO_4$ [3] as well as cubic spinels AB_2O_4 with a magnetic ion on the A -site [4–7]. The perfect diamond lattice is bipartite and unfrustrated, expected to order into a collinear antiferromagnetic ground state if only nearest-neighbor interactions (J_1) are considered [8]. However, magnetic frustration can arise if interactions with the twelve next-nearest-neighbors (J_2) are included, or if distortion lowers the symmetry from cubic. This may give rise to exotic magnetic behaviour including spiral spin-liquid states [9, 10] or topological paramagnetism [11–13].

The diamond lattice can also be viewed as a truncated version of the $\mathcal{H}\langle 0\rangle$ ‘hyperhoneycomb’ structure of β - Li_2IrO_3 , using nomenclature for the so-called harmonic honeycomb series [14]. This ‘truncation’ is carried out by removing the black links (parallel to c) from the $N = 0$ structure, as shown in Fig. 1. N stands for the number of complete hexagonal rows along the c -axis before a change of orientation of the hexagons. Alternatively, $N + 1$ is the number of black (c -axis) links between changes of orientation [15]; as such, we propose the notation $\mathcal{H}\langle-1\rangle$ for the diamond lattice. Magnetic frustration in materials with the $\mathcal{H}\langle-1\rangle$ connectivity is probable in crystal symmetries lower than cubic. Such a ‘stretched’ diamond lattice has previously been described for tetragonal $LiYbO_2$, which

has an incommensurate spiral magnetic order [16], and $NaCeO_2$ with A -type antiferromagnetic order [17]. The $\mathcal{H}\langle-1\rangle$ network also occurs in the fergusonite (monoclinic, M) and scheelite (tetragonal, T) polymorphs of the oxides $LnTaO_4$ and $LnNbO_4$, of which the former is the subject of this experimental study.

Rare-earth orthoniobates $LnNbO_4$ and orthotantalates $LnTaO_4$ ($Ln = Y, La-Lu$) are of wide interest as a result of their luminescent [18, 19], proton-conducting [20], oxide-ion-conducting [21] and dielectric properties [22]. The tantalates have also been proposed as thermal barrier coatings for gas turbines [23]. The niobates and tantalates share two common crystallographic polymorphs: fergusonite ($I2/a$, monoclinic, M) and scheelite ($I4_1/a$, tetragonal, T) [24–31]. Additionally, the tantalates may crystallize in different monoclinic and tetragonal (M' , T') phases depending on the synthesis conditions. The T phase has been observed using *in situ* diffraction experiments, but it rapidly converts to the M phase upon cooling and cannot be isolated at room temperature. The M - T transformation temperature occurs at 1325–1410 °C for the tantalates and 500–800 °C for the niobates; within each series this transition temperature increases with decreasing Ln^{3+} radius [32]. The two monoclinic polymorphs of $LnTaO_4$ are closely related: to change from M to M' only involves halving the b -axis and removing the body-centering [27, 33]. The metal–oxygen coordination polyhedra (distorted square antiprisms for Ln^{3+} and distorted octahedra for Ta^{5+}) are approximately the same in both phases [28]. However, the change of centering means that the M and M' structures have significantly different arrangements of the polyhedral building blocks: distinct layers perpendicular to a in the M' phase, but a different, non-layered arrangement in the M phase [29] as shown in Fig. 2. The arrangement of lanthanide ions in the M phase is equivalent to the stretched diamond or $\mathcal{H}\langle-1\rangle$ network as discussed earlier.

* ne281@cam.ac.uk

† Present address: School of Physics and Astronomy, University of Edinburgh, Peter Guthrie Tait Road, Edinburgh, EH9 3FD, UK

‡ sed33@cam.ac.uk

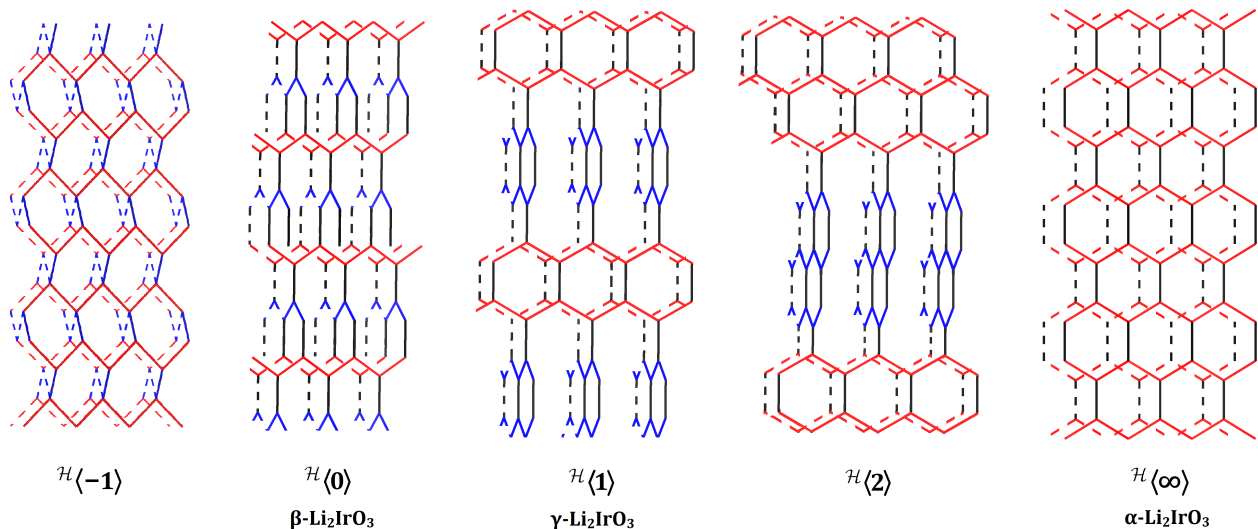


FIG. 1. The $N = -1, 0, 1, 2$, and ∞ members of the harmonic honeycomb series, where N represents the number of complete honeycomb rows along the c -axis before a change of orientation of the honeycomb planes. After Modic *et al.* [14].

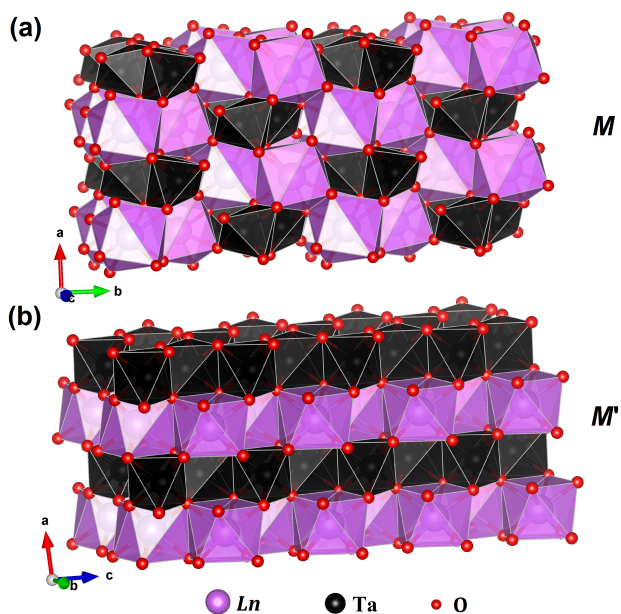


FIG. 2. Crystal structures of (a) M ($I2/a$), (b) M' ($P2/c$) phases of $LnTaO_4$.

Numerous diffraction studies have been carried out on the lanthanide niobates and tantalates with both powder and single-crystal samples [31, 33–36] but their magnetic properties are under-researched by comparison. In 1965, Wang and Gravel measured the susceptibilities of M -GdNbO₄ and M -NdNbO₄ at 5–750 K and found paramagnetism and antiferromagnetism respectively, with $T_N = 25$ K for NdNbO₄ [37]. Cashion *et al.* investigated M - Ln NbO₄ with $Ln = Nd, Gd, Tb, Dy, Ho, Er$ and Yb

but found magnetic transitions only below 2 K (i.e. no feature at 25 K in NdNbO₄), again with negative Curie-Weiss temperatures indicating antiferromagnetic interactions [38]. At around the same time Starovoitov *et al.* independently measured isothermal magnetisation on M - Ln NbO₄ with $Ln = Nd, Eu, Sm, Gd, Dy, Ho$ and Yb, finding evidence for single-ion anisotropy in all samples except GdNbO₄, as expected for a f^7 system with $L = 0$ [39]. Tsunekawa *et al.* measured the susceptibility of single crystals of selected M - Ln NbO₄ ($Ln = Nd, Gd, Ho$) and M - Ln TaO₄ ($Ln = Nd, Ho, Er$) in the range 4.2 to 300 K; again $\theta_{CW} < 0$ for all compounds, with no magnetic ordering observed. Deviations from the Curie-Weiss law at low temperatures and a marked anisotropy in the susceptibility were observed in all cases except GdNbO₄; this behaviour was attributed to a crystal field with its principal direction along the c -axis, with the greatest effect occurring for $Ln = Nd$ [40, 41].

This article reports the bulk magnetic characterisation of eight powder samples in the series M - Ln TaO₄, $Ln = Nd, Sm, Eu, Gd, Tb, Dy, Ho, Er$. The compounds with the larger lanthanides $Ln = La, Ce$ and Pr do not form the M structure [31, 33, 42] and were therefore excluded from this study. We confirm the absence of long-range ordering in NdTaO₄, HoTaO₄ and ErTaO₄ above 2 K, extending the range investigated in a previous study [41]. TbTaO₄ was also studied using high-resolution powder neutron diffraction. It exhibits a transition at $T = 2.25$ K to a commensurate antiferromagnetic structure with $\vec{k} = 0$. No magnetic transitions occurred above 2 K for the remaining samples with $Ln = Sm, Eu, Gd, Dy$. These measurements indicate the presence of magnetic frustration in M - Ln TaO₄ and lay the foundations for future investigations, as possible hosts for novel magnetic states as predicted for the $\mathcal{H}(-1)$ lattice.

II. EXPERIMENTAL

Polycrystalline samples of M - Ln TaO₄ were synthesized according to a ceramic procedure, starting from Ta₂O₅ (Alfa Aesar, 99.993 %) and Ln_2 O₃ ($Ln = Nd, Sm, Eu, Gd, Dy, Ho, Er, Y$) or Tb₄O₇ (Alfa Aesar; all lanthanide oxides ≥ 99.99 %). Lanthanide oxides were dried in air at 800 °C overnight before weighing. For each compound, 1:1 molar amounts of the reagents were ground with an agate pestle and mortar, pressed into a 13 mm pellet and placed in an alumina crucible. Pellets were fired for 3 x 24 h at 1500 °C in air with intermediate regrinding. The exception was ErTaO₄, which first formed the M' phase ($P2/c$) at 1500 °C and required an additional 2 x 24 h at an elevated temperature, 1600 °C, to form solely the desired M phase. Heating and cooling rates were 3 °C per minute.

Powder X-ray diffraction (PXRD) was carried out at room temperature on a Bruker D8 diffractometer (Cu K α , $\lambda = 1.541$ Å) in the range $10 \leq 2\theta(^{\circ}) \leq 70$ with a step size of 0.02°, 0.6 seconds per step. Rietveld refinements [43] were carried out using TOPAS [44] with a Chebyshev polynomial background and a modified Thompson-Cox-Hastings pseudo-Voigt peak shape [45]. VESTA [46] was used for crystal structure visualisation and production of figures.

Powder neutron diffraction (PND) was carried out on a 3 g sample of TbTaO₄ on the D1B and D2B diffractometers (high intensity and high resolution respectively), ILL, Grenoble, using an Orange cryostat ($1.5 \leq T(K) \leq 300$). Wavelengths were refined to 2.52461(6) Å for D1B and 1.594882(10) Å for D2B. Determination of the magnetic structure was carried out using FULLPROF [47] and TOPAS [44]. The background was modelled with a Chebyshev polynomial and the peak shape modelled with a modified Thompson-Cox-Hastings pseudo-Voigt function with axial divergence asymmetry [45].

DC magnetisation was measured on warming on a Quantum Design MPMS 3 at a field of 500 Oe in the temperature range $2 \leq T(K) \leq 300$, after cooling from 300 K in zero applied field (ZFC) or 500 Oe applied field (FC). Isothermal magnetisation was measured on a Quantum Design PPMS DynaCool using the ACMS-II option in the field range $\mu_0 H = 0-9$ T. In a low field, up to 500 Oe, the $M(H)$ curve was linear and the susceptibility could therefore be approximated by $\chi(T) = M/H$.

Zero-field heat capacity of TbTaO₄ was measured on the PPMS in the range $1.8 \leq T(K) \leq 30$. The sample was mixed with an equal mass of Ag powder (Alfa Aesar, 99.99 %, -635 mesh) to improve thermal conductivity, then pressed into a 1 mm thick pellet for measurement. Apiezon N grease was used to provide thermal contact between the sample platform and the pellet. Fitting of the relaxation curves was done using the two-tau model. The contribution of Ag to the total heat capacity was subtracted using scaled values from the literature [48]. The TbTaO₄ lattice contribution was estimated and subtracted using a Debye model with $\theta_D = 370$ K [49].

III. RESULTS

A. Crystal structure

For $Ln = Nd-Ho$ & Y, a small amount, < 5 wt %, of the metastable M' -phase (space group $P2/c$; Fig. 2(b)) was formed in the first heating step but disappeared on further heating. ErTaO₄ formed only the M' phase at 1500 °C but formed the desired M phase after heating at 1600 °C. Attempts to produce M -YbTaO₄ by the same methods were unsuccessful, in agreement with previous authors who found that making this phase requires quenching from high temperature and/or pressure [23, 50]. Synthesis of YbTaO₄ by spark plasma sintering (SPS) was attempted as reported in the literature (various experiments with $T \leq 1600$ °C, $p \leq 500$ bar, fast or slow cooling [51]) but was unsuccessful, producing only the M' phase with unreacted Yb₂O₃ and Ta₂O₅. It thus appears that the relative stability of M' over M increases across the lanthanide series with decreasing ionic radius, since LuTaO₄ also favours the M' phase [23] and the solid solution $Y_{1-x}Yb_x$ TaO₄ favours M' when $x \geq 0.5$ [52].

PXRD and Rietveld refinement indicated that each sample eventually formed a single phase with the monoclinic M - Ln TaO₄ crystal structure, space group $I2/a$, shown in Fig. 2(a). Unit cell dimensions and the Ln^{3+} and Ta⁵⁺ atomic positions were refined, but the positions of O²⁻ ions were fixed at values taken from neutron diffraction of NdTaO₄ [34] because of the low X-ray scattering power of oxygen compared with the heavier metal ions. Refinement of fractional site occupancies with fixed overall stoichiometry indicated that there was no disorder between the Ln^{3+} and Ta⁵⁺ cations. This result is as expected because 6-coordinate Ta⁵⁺ is much smaller than any of the 8-coordinate lanthanide ions [53]. Refined unit cell parameters (Supplemental Material) are in good agreement with literature results [23, 25, 34]. A representative Rietveld fit is shown in Fig. 3; fits for the remaining compounds are in the Supplemental Material. The unit cell volume decreased linearly with decreasing lanthanide ionic radius (Fig. 4).

We obtained high-resolution powder neutron diffraction (PND) data for the paramagnetic phase of TbTaO₄ at 30 K using the D2B beamline at the ILL [54]. The measurements confirmed that the nuclear structure of TbTaO₄ is consistent with previous reports for Ln TaO₄ compounds [25, 31, 34]. Fig. 5(a) shows a Rietveld refinement of PND data collected at $T = 30$ K with $\lambda \approx 1.59$ Å. Interatomic distances were also obtained. The Ta⁵⁺ ions are surrounded by four shorter and two longer Ta-O bonds, forming octahedra distorted by a second-order Jahn-Teller effect [31], while the Tb³⁺ ions are 8-coordinate. The refined bond lengths are listed in Table I.

In addition, we were able to resolve and follow the evolution of the nuclear structure with temperature using PND data collected on the D1B beamline. No phase transitions were observed in the temperature range 3–300 K.

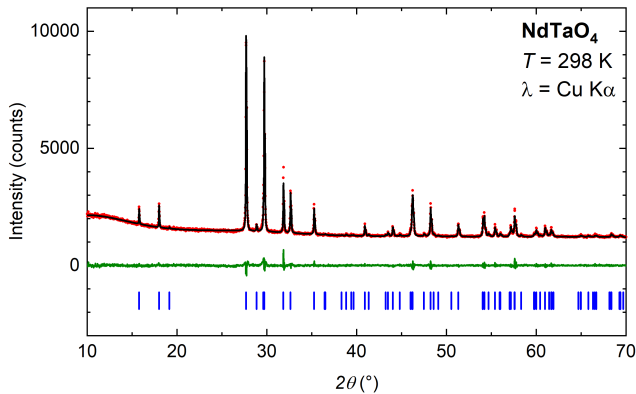


FIG. 3. Room temperature PXRD pattern for NdTaO_4 : red dots – experimental data; black line – calculated intensities; green line – difference pattern; blue tick marks – Bragg reflection positions.

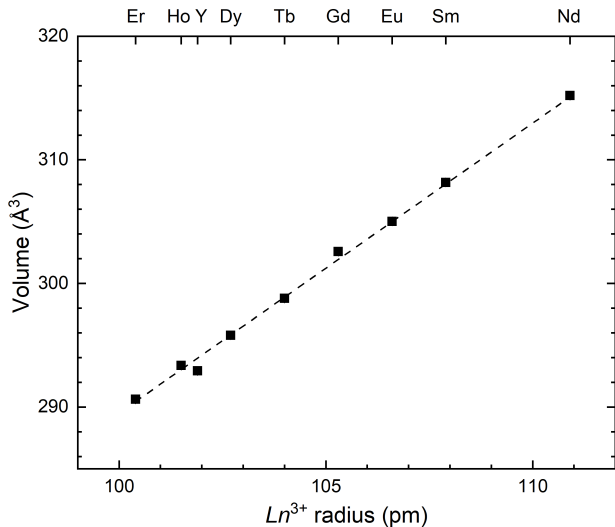


FIG. 4. Unit cell volumes of $M\text{-LnTaO}_4$ compounds after PXRD and Rietveld refinement with dashed line of best fit to guide the eye. Error bars are smaller than the datapoints. Ionic radius is for an 8-coordinate ion [53].

TABLE I. Refined interatomic distances for TbTaO_4 from PND data collected at 1.59 \AA (D2B, ILL).

Atoms		Distance / \AA	
		$T = 1.5 \text{ K}$	$T = 30 \text{ K}$
Ta–O(2)	x 2	1.877(4)	1.871(4)
Ta–O(1)	x 2	1.938(4)	1.945(3)
Ta–O(1)	x 2	2.301(4)	2.297(4)
Tb–O(2)	x 2	2.314(3)	2.311(2)
Tb–O(1)	x 2	2.342(4)	2.342(3)
Tb–O(2)	x 2	2.376(4)	2.379(3)
Tb–O(1)	x 2	2.500(4)	2.492(3)

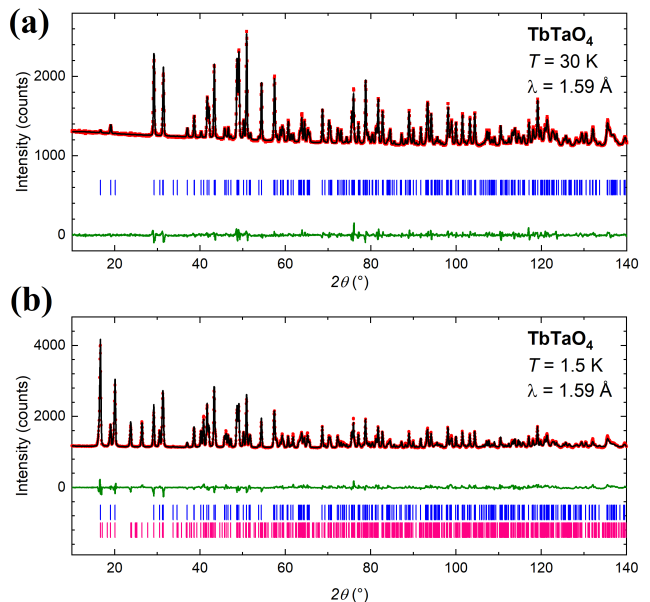


FIG. 5. PND data for TbTaO_4 collected at $\lambda = 1.59 \text{ \AA}$ on the D2B diffractometer: (a) 30 K, (b) 1.5 K. Red dots – experimental data; black line – calculated intensities; green line – difference pattern; tick marks – nuclear (blue) and magnetic (pink) Bragg reflection positions.

The lattice parameters were constant between 3 and 50 K and then varied smoothly between 50 and 300 K. Small decreases in a and β on warming were offset by increases in b and c , Fig. S1. There were similar subtle changes to the atomic fractional coordinates between 50 and 300 K (Figs S2 and S3).

B. Bulk magnetic properties

1. Magnetic susceptibility

The zero-field-cooled (ZFC) magnetic susceptibility at 500 Oe for each LnTaO_4 compound (Fig. 6) was fitted to the Curie-Weiss law, $\chi = C/(T - \theta_{\text{CW}})$. The effective magnetic moment was calculated from the experimental data using $\mu_{\text{eff}}/\mu_{\text{B}} = \sqrt{8C}$ and compared to the theoretical paramagnetic moment $g_J\sqrt{J(J+1)}$. Linear fitting was carried out in both high-temperature and low-temperature regimes to account for different thermal population of excited states at higher temperatures. The results from the two fitting regimes (Table II) are significantly different, indicating that crystal field effects at high temperatures may influence the magnetic correlations and thus the susceptibility. The low-temperature fits are therefore more likely to represent the true properties of these materials [55, 56]. The magnetic moments derived from Curie-Weiss fitting agree well with the expected free-ion moments as well as those obtained by Tsunekawa *et al.* [41].

No sharp peaks in the susceptibility were observed for any of the eight compounds except TbTaO₄ ($T_N = 2.9$ K). Field-cooled (FC) susceptibility at 500 Oe was also measured on TbTaO₄ and found to be identical to the ZFC data, suggesting three-dimensional antiferromagnetic ordering without glassiness.

The shape of the EuTaO₄ susceptibility curve resembles that of other Eu-containing ceramics and is believed to result from van Vleck paramagnetism, i.e. non-zero occupation of low-lying magnetic excited states 7F_1 to 7F_6 [57–59]. The inverse susceptibility plot is linear at 200–300 K, but applying the Curie-Weiss law produced unrealistically large values of the magnetic moment and Curie-Weiss temperature ($5 \mu_B$ and -340 K respectively) as a result of the population of excited states. No fitting was carried out at low temperature as the plot of $\chi^{-1}(T)$ was not linear.

The susceptibility of SmTaO₄ at high temperatures shows a large contribution from temperature-independent paramagnetism: both $\chi(T)$ and $\chi^{-1}(T)$ tend towards a constant value, without becoming linear. Curie-Weiss fitting was therefore carried out in the low-temperature range only. The calculated effective magnetic moment is $0.72 \mu_B$, slightly lower than the expected free ion value of $0.85 \mu_B$, likely owing to the large crystal field splitting in the $J = 5/2$ ground state multiplet of Sm³⁺ [55, 59]. The negative Curie-Weiss temperature indicates antiferromagnetic interactions between adjacent Sm³⁺ ions, as indeed is the case for all the remaining LnTaO₄ samples.

2. Isothermal magnetisation

Fig. 7 shows the isothermal magnetisation at 2 K for the LnTaO₄ compounds. For the samarium and europium compounds, the magnetisation plots initially curve upwards then become linear above 3 T without saturating. In all other samples the magnetisation, plotted in units of Bohr magnetons per formula unit ($\mu_B/\text{f.u.}$), tends towards a saturation value M_{sat} at high field. The expected value of M_{sat} depends on both the identity of the lanthanide ion and the extent of single-ion anisotropy – the tendency for a spin to align along a particular local axis or local plane. For example, compounds containing Gd³⁺ typically display Heisenberg-type behaviour with saturation at the maximum value of $g_J \cdot J = 7 \mu_B/\text{f.u.}$, while systems with Ising (easy-axis) or XY (easy-plane) behaviour are expected to saturate around $g_J \cdot J/2$ or $2g_J \cdot J/3$ respectively. However, individual systems may vary from these values depending on the local symmetry of the lanthanide ion coordination environment [60, 61]. The experimental values of $M_{2\text{K},9\text{T}}$ for each compound and the calculated $g_J \cdot J$ for each lanthanide ion are given in Table II.

The experimental data indicate that the compounds with $Ln = \text{Nd, Tb, Dy, Ho}$ and Er all show some degree of local anisotropy; further experiments such as

neutron diffraction would be needed to investigate this further. However, neutron absorption would make it difficult to measure the anisotropy in DyTaO₄ without an isotopically enriched sample. A previous study on large single crystals of LnTaO₄ ($Ln = \text{Nd, Ho, Er}$) also found substantial anisotropy in the magnetic susceptibility measured along the different crystal axes [41]. In that study, the plots of inverse susceptibility along each crystal axis have the same gradient but different x -intercepts, i.e. Curie-Weiss temperatures: for example, NdTaO₄, which showed the greatest anisotropy, had $\theta_{\text{CW}} = -7, -56$ and -52 K along the a, b and c axes respectively.

3. Specific heat

The magnetic heat capacity for TbTaO₄ shows a sharp λ -type transition at $T = 2.25$ K, where there is a corresponding feature in the plot of $d(\chi T)/dT$ [62], Fig. 8. This provides further evidence for three-dimensional antiferromagnetic ordering as deduced from the susceptibility data. The magnetic entropy associated with the transition was obtained by integration of the heat capacity curve over the full temperature range (1.8–30 K) and found to approach $2 \text{ J mol}^{-1} \text{ K}^{-1}$ (Fig. 8, inset). Since the expected maximum entropy is $R \ln 2 = 5.76 \text{ J mol}^{-1} \text{ K}^{-1}$ for Ising spins with effective spin of $1/2$, the remaining entropy change is assumed to occur below the lowest temperature measured (1.8 K) which has non-zero C_{mag}/T and is close to T_N .

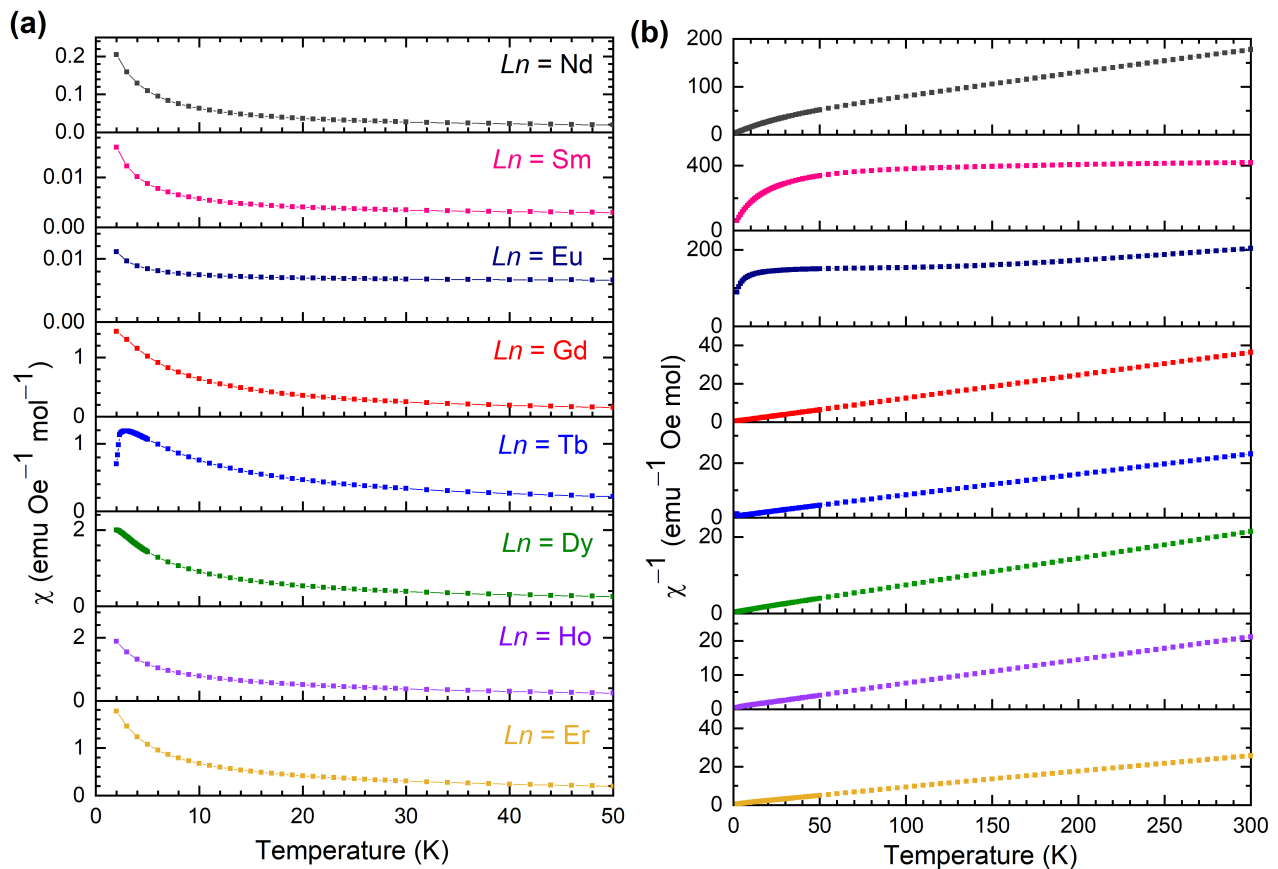
C. Magnetic structure of TbTaO₄

We obtained high-resolution PND data for the magnetic phase of TbTaO₄ at 1.5 K using the D2B beamline at the ILL [54]. Variable-temperature PND was also carried out on the D1B beamline in order to track the evolution of the magnetic structure with temperature. On cooling below $T = 2.3$ K, magnetic Bragg peaks were observed to appear and increase in intensity as the temperature was lowered. No discernible diffuse scattering was observed above this temperature. The magnetic peaks could be indexed to a commensurate magnetic cell with $\vec{k} = 0$ in the magnetic space group $14.77 (P2_1'/c)$. Refinement of the magnetic structure using TOPAS (Fig. 5(b)) shows Tb moments parallel to the a -axis in A -type antiferromagnetic order: the moments coalign within the ac plane, forming ferromagnetic slabs coupled antiferromagnetically along b , Fig. 9(a). The structure is similar to that of NaCeO₂ which has the same A -type order but Ce³⁺ moments aligned along the tetragonal c -axis [17]. Further details of the magnetic structure may be found in the Supplemental Material (Table S3).

The refined ordered moment is plotted as a function of temperature in Fig. 10, showing good agreement with the transition temperature found by heat capacity and magnetic susceptibility. At 1.5 K the moment of

TABLE II. Bulk magnetic properties of M - Ln TaO₄, $Ln = \text{Nd, Sm, Eu, Gd, Tb, Dy, Ho, Er}$.

Ln	$g_J\sqrt{J(J+1)}$	High T fit (K)	μ_{eff} (μ_B)	θ_{CW} (K)	Low T fit (K)	μ_{eff} (μ_B)	θ_{CW} (K)	$g_J J$	$M_{2\text{K},9\text{T}}$ ($\mu_B/\text{f.u.}$)
Nd	3.62	150–300	4.08(8)	-71.3(14)	30–50	3.27(7)	-19.7(4)	3.29	1.312(26)
Sm	0.85	N/A	N/A	N/A	2–8	0.724(29)	-2.33(19)	0.71	0.0749(15)
Eu	0	N/A	N/A	N/A	N/A	N/A	N/A	0	0.1037(21)
Gd	7.94	150–300	8.20(16)	-6.42(13)	10–50	8.09(16)	-2.82(6)	7	6.88(14)
Tb	9.72	150–300	10.33(21)	-12.75(25)	10–50	9.92(20)	-6.50(13)	9	5.48(11)
Dy	10.65	150–300	10.70(21)	-6.44(13)	10–50	10.57(21)	-6.09(12)	10	6.00(12)
Ho	10.61	150–300	10.90(22)	-14.50(29)	10–50	10.70(21)	-8.20(16)	10	6.72(13)
Er	9.58	150–300	9.95(20)	-19.1(4)	10–50	9.50(19)	-7.03(14)	9	5.98(12)

FIG. 6. (a) ZFC susceptibility, (b) reciprocal susceptibility χ^{-1} as a function of temperature for the Ln TaO₄ samples with $Ln = \text{Nd, Sm, Eu, Gd, Tb, Dy, Ho}$ and Er.

7.5(4) μ_B/Tb^{3+} is slightly below the expected value of 9 μ_B .

The nearest-neighbor superexchange in TbTaO₄ follows Tb–O–Tb pathways. These pathways may be divided into J_{1a} and J_{1b} according to the different Tb–O bond lengths. Figs 9(b) and 9(c) highlight these two interactions: J_{1a} vectors (shorter) in the ab plane and J_{1b} vectors (longer) in the bc plane. In the mean-field approximation, the average exchange interaction \bar{J}_1 may be calculated as $\bar{J}_1 = [3k_B\theta_{\text{CW}}]/[2nJ(J+1)]$, where J is

the spin quantum number and n the number of nearest-neighbor spins [63]. Using an effective spin of 1/2 for the Tb^{3+} ion [64] we estimate $\bar{J}_1 \approx 3.3$ K, of the same order as the Néel temperature. However, the mean-field approximation may not be completely valid given the significant single-ion anisotropy observed in $M(H)$ data.

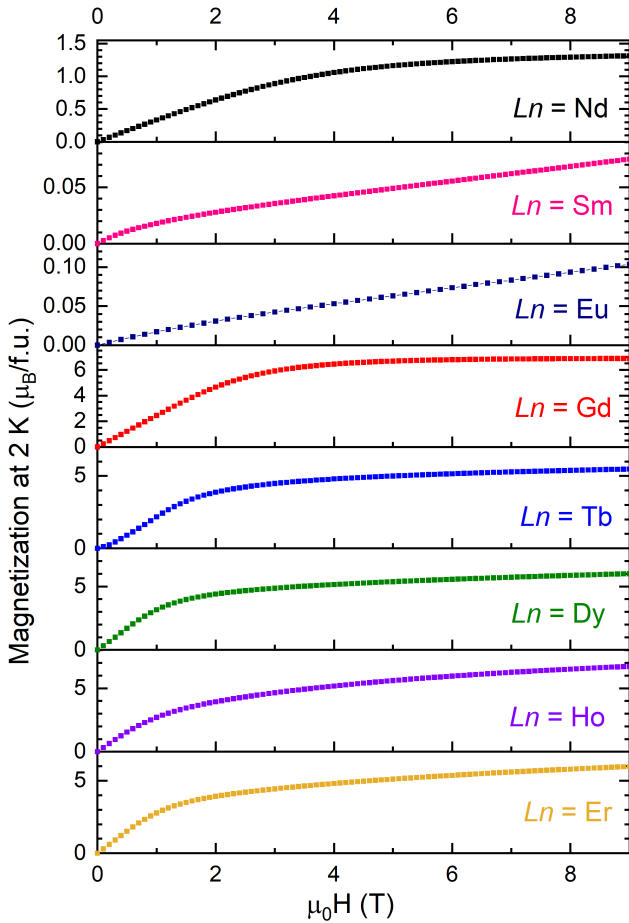


FIG. 7. Magnetisation as a function of applied field for the $LnTaO_4$ samples with $Ln = Nd, Sm, Eu, Gd, Tb, Dy, Ho$ and Er .

IV. DISCUSSION

We report the magnetic behaviour of a new family of Ln^{3+} oxides containing a stretched diamond lattice. Other such materials include the alkali metal-lanthanide oxides $NaLnO_2$ ($Ln = Ce, Nd, Sm, Eu, Gd$) and $LiLnO_2$ ($Ln = Er, Yb$), which crystallize in the tetragonal space group $I4_1/amd$ [16, 17, 65]. The observation of the stretched diamond lattice in monoclinic $LnTaO_4$ materials provides a new opportunity to study the interplay of the crystal electric field with competing J_1 and J_2 magnetic interactions. In particular, while $TbTaO_4$ exhibits long-range A -type antiferromagnetic order similar to that of $NaCeO_2$ [17], the other materials with $Ln = Nd-Er$ do not order at $T \geq 2$ K. The absence of ordering above 2 K, in contrast to e.g. $NaLnO_2$ (Ce, Gd antiferromagnetic; Nd ferromagnetic [65]) suggests the potential for novel magnetic states at low temperature.

We link the stretched diamond lattice to the wider harmonic honeycomb family of magnetic networks [14] by extending the series to $\mathcal{H}\langle -1 \rangle$. Like the materials in the wider series $\mathcal{H}\langle N \rangle$, which include $YbCl_3$ [66] and the $\alpha,$

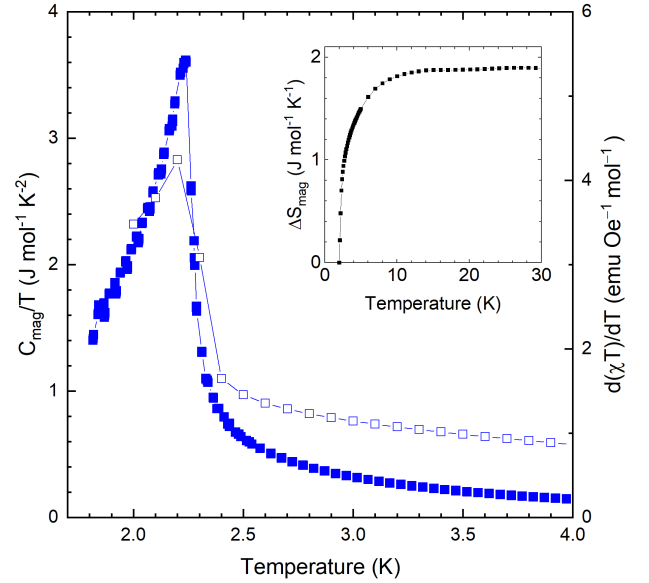


FIG. 8. Magnetic heat capacity (filled symbols) and $d(\chi T)/dT$ vs T (open symbols) for $TbTaO_4$. Inset: magnetic entropy ΔS_{mag} obtained by integration of C_{mag}/T .

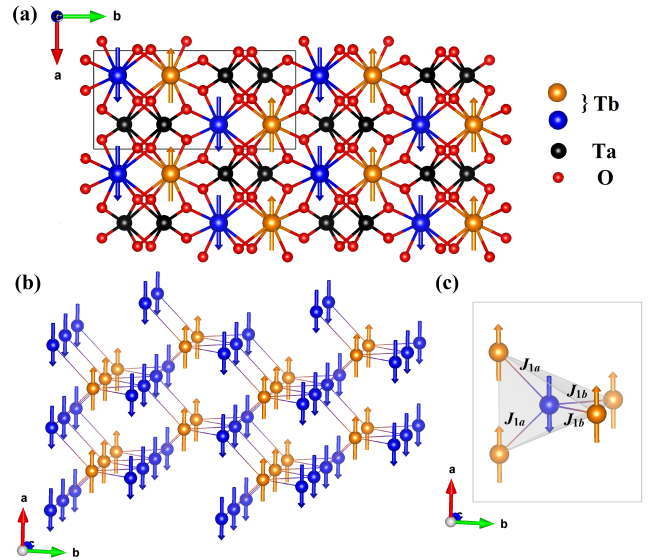


FIG. 9. Magnetic structure of $TbTaO_4$ from refinement at 1.5 K: (a) all atoms, (b) Tb spins only, (c) nearest-neighbor interactions.

β and γ polymorphs of Li_2IrO_3 [15], magnetism on the $\mathcal{H}\langle -1 \rangle$ lattice is governed by the interplay of nearest-neighbor and next-nearest-neighbor interactions. Describing the stretched diamond lattice as $\mathcal{H}\langle -1 \rangle$ provides a useful framework to draw parallels between different materials within the harmonic honeycomb series.

There are two parameters which are useful for comparing the level of stretching in different $\mathcal{H}\langle -1 \rangle$ lattices.

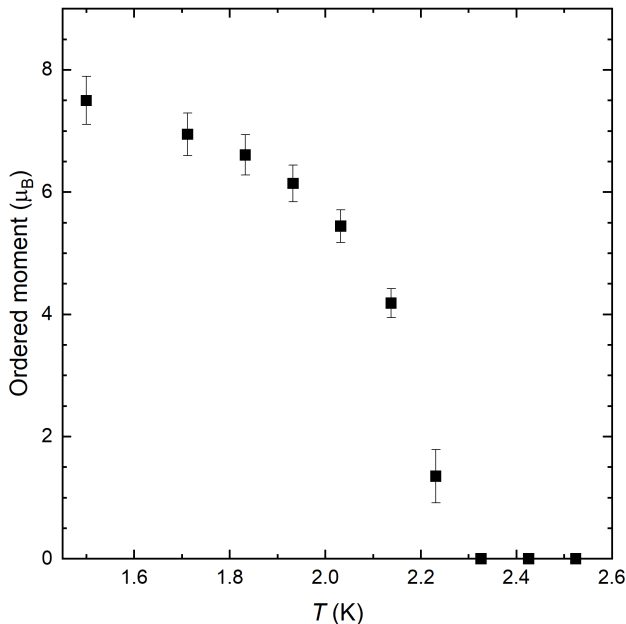


FIG. 10. Evolution of the Tb^{3+} ordered magnetic moment as a function of temperature from variable-temperature PND.

The first is the angle or angles around each lattice vertex. In an ideal cubic diamond lattice, all these angles are equal at 109.5° . When the diamond lattice is distorted, the number of different angles increases: there are two in tetragonal, three in hexagonal, and four in monoclinic symmetry. We compare the average deviation from ideal tetrahedral geometry by defining a parameter d_a , the angle distortion index, as follows:

$$d_a = \frac{\phi_{\max} - \phi_{\min}}{\bar{\phi}} \quad (1)$$

where ϕ_{\max} and ϕ_{\min} are the largest and smallest angles respectively, and $\bar{\phi}$ is the mean angle. Secondly, we define a bond distortion index d_b in a similar way:

$$d_b = \frac{r_2 - r_1}{\frac{1}{2}(r_1 + r_2)} \quad (2)$$

where r_1 and r_2 are the two ‘nearest-neighbor’ interaction distances (red and blue in Fig. 1). These distances are equal in the case of the undistorted (cubic) or the tetragonal or hexagonal stretched diamond lattices, but not in monoclinic materials such as the tantalates. Table III lists the distortion indices for several magnetic materials containing the $\mathcal{H}\langle-1\rangle$ lattice. Values were calculated using the program VESTA [46] to examine the published crystal structures.

The presence or absence of bond or angular distortion in the $\mathcal{H}\langle-1\rangle$ lattice thus appears to have no clear impact on the magnetic properties, with ordering of TbTaO_4 occurring at a similar temperature to NaNdO_2 and NaGdO_2 despite the higher symmetry of NaLnO_2 . The

absence of long-range order for the other LnTaO_4 compounds further demonstrates the non-trivial role of distortion in the low-temperature magnetic properties of the $\mathcal{H}\langle-1\rangle$ harmonic honeycombs.

Finally, we note that LaTaO_4 , while not forming the fergusonite structure type, nonetheless displays rich structural phase behaviour including an incommensurate-commensurate phase transition at 483 K coinciding with a dielectric anomaly [71, 72]. Dias *et al.* have made comparative dielectric measurements on LaTaO_4 ($P2_1/c$), NdTaO_4 ($I2/a$), and DyTaO_4 and LuTaO_4 ($P2/a$). Despite the differences in structure, the dielectric constants of the Nd, Dy and Lu tantalates are $\leq 25\%$ smaller than that of LaTaO_4 and still within the range of useful microwave materials [73]. Considering that Nd^{3+} and Dy^{3+} have non-zero magnetic moments, there is a possibility of coupling between magnetic and electric properties which should be investigated in these and the other magnetic tantalates.

V. CONCLUSIONS

Polycrystalline samples of LnTaO_4 ($\text{Ln} = \text{Nd}, \text{Sm}, \text{Er}, \text{Y}$) in the monoclinic M , or fergusonite, structure type have been synthesized using a ceramic procedure. The trivalent lanthanide ions in the crystal structure form a three-dimensional net equivalent to an elongated or ‘stretched’ diamond lattice. This lattice can also be considered a truncated form of the hyperhoneycomb lattice $\mathcal{H}\langle 0\rangle$, part of the harmonic honeycomb series, and is therefore denoted $\mathcal{H}\langle-1\rangle$. Bulk magnetic characterisation of the tantalate samples confirms a previous literature result for $\text{Ln} = \text{Nd}, \text{Ho}, \text{Er}$, and reveals that the remaining compounds do not order above 2 K with the exception of TbTaO_4 , which has $T_N = 2.25$ K. High-resolution PND was used to examine the paramagnetic and magnetic phases of TbTaO_4 , revealing that it forms a commensurate $\vec{k} = 0$ magnetic unit cell. The Tb moments lie parallel to the a -axis in A -type antiferromagnetic order. Future work will include specific heat measurements at $T < 2$ K in order to search for further magnetic transitions and investigate the magnetic ground states of the remaining tantalates.

ACKNOWLEDGMENTS

N.D.K. thanks Sundeep Vema for carrying out the reactions at 1600 °C, Farheen Sayed for the SPS experiments and James Analytis for technical advice on producing Fig. 1. We acknowledge funding from the EPSRC (EP/T028580/1, EP/R513180/1, EP/M000524/1).

Supplementary tables and figures are available at (DOI). Neutron diffraction data are available at reference [54]. The authors gratefully acknowledge the technical and human support provided at the Institut Laue-Langevin (ILL), Grenoble. Additional data related to

TABLE III. Distortion indices and magnetic behaviour of materials with the stretched diamond lattice.

Crystal symmetry	Formula	Space group	d_a (%)	d_b (%)	T_N (K)	Magnetic structure
Cubic	CoRh ₂ O ₄ [7]	$Fd\bar{3}m$	0	0	25	Néel AFM $\parallel \langle 100 \rangle$
	MnAl ₂ O ₄ [4]	$Fd\bar{3}m$	0	0	40	Canted AFM
	FeAl ₂ O ₄ [4]	$Fd\bar{3}m$	0	0	12	Spin glass
	CoAl ₂ O ₄ [4]	$Fd\bar{3}m$	0	0	4.8	Spin glass
	CuAl ₂ O ₄ [67]	$Fd\bar{3}m$	0	0	< 0.4	No long range order
	FeSc ₂ S ₄ [68]	$Fd\bar{3}m$	0	0	< 0.05	Spin-orbital liquid
	MnSc ₂ S ₄ [9]	$Fd\bar{3}m$	0	0	2.3, 1.9	Long-range spiral order
Tetragonal	CuRh ₂ O ₄ [7]	$I4_1/amd$	7	0	24	Incommensurate helical order
	NiRh ₂ O ₄ [13]	$I4_1/amd$	3	0	< 0.1	No long range order
	NaCeO ₂ [17]	$I4_1/amd$	42	0	3.18	Néel AFM $\parallel c$
	NaNdO ₂ [65]	$I4_1/amd$	41	0	2.4	FM
	NaGdO ₂ [65]	$I4_1/amd$	40	0	2.4	AFM
	LiYbO ₂ [16]	$I4_1/amd$	41	0	0.45	Incommensurate helical order
	KRuO ₄ [2]	$I4_1/a$	42	0	22.4	Néel AFM $\parallel c$
	KOsO ₄ [3]	$I4_1/a$	39	0	35	Néel AFM $\parallel c$
Hexagonal	β -KTi(C ₂ O ₄) ₂ ·2H ₂ O [1]	$P6_222$	34	0	28	Coplanar AFM
Monoclinic	NdTaN ₂ O ₄	$I2/a$	42	2.9	< 2	No long range order
	GdTaN ₂ O ₄	$I2/a$	41	2.6	< 2	No long range order
	TbTaN ₂ O ₄	$I2/a$	41	2.2	2.25	Néel AFM $\parallel a$
	DyTaN ₂ O ₄	$I2/a$	41	4.1	< 2	No long range order
	HoTaN ₂ O ₄	$I2/a$	41	4.1	< 2	No long range order
	ErTaN ₂ O ₄	$I2/a$	41	3.9	< 2	No long range order
	NdNbO ₄ [35, 38]	$I2/a$	40	1.1	< 1	No long range order
	GdNbO ₄ [38, 69]	$I2/a$	39	0.7	1.67	AFM
	TbNbO ₄ [25, 38]	$I2/a$	39	1.0	1.82	AFM
	DyNbO ₄ [25, 38]	$I2/a$	39	0.3	1.6	AFM
	HoNbO ₄ [35, 38]	$I2/a$	39	1.1	< 1	No long range order
	ErNbO ₄ [25, 38]	$I2/a$	38	0.6	< 1.3	No long range order
	YbNbO ₄ [35, 38]	$I2/a$	38	1.2	< 1.3	No long range order
	Pr(BO ₂) ₃ [70]	$C2/c$	61	12.1	–	Singlet ground state
	Nd(BO ₂) ₃ [70]	$C2/c$	61	12.0	< 0.4	No long range order
Gd(BO ₂) ₃ [70]	$C2/c$	64	12.6	1.1	AFM	
Tb(BO ₂) ₃ [70]	$C2/c$	66	13.1	1.95, 1.05	Undetermined	

this publication are available in the Cambridge University Repository at (DOI).

- [1] A. H. Abdeldaim, T. Li, L. Farrar, A. A. Tsirlin, W. Yao, A. S. Gibbs, P. Manuel, P. Lightfoot, G. J. Nilsen, and L. Clark, Realising square and diamond lattice $S = 1/2$ Heisenberg antiferromagnet models in the α and β phases of the coordination framework, KTi(C₂O₄)₂· x H₂O, Phys. Rev. Mater. **4**, 104414 (2020).
- [2] C. A. Marjerrison, C. Mauws, A. Z. Sharma, C. R. Wiebe, S. Derakhshan, C. Boyer, B. D. Gaulin, and J. E. Greedan, Structure and Magnetic Properties of KRuO₄, Inorg. Chem. **55**, 12897 (2016).
- [3] S. Injac, A. K. L. Yuen, B. J. Kennedy, M. Avdeev, and F. Orlandi, Structural and magnetic studies of KOsO₄, a 5d¹ quantum magnet oxide, Phys. Chem. Chem. Phys. **21**, 7261 (2019).
- [4] N. Tristan, J. Hemberger, A. Krimmel, H. A. Krug Von Nidda, V. Tsurkan, and A. Loidl, Geometric frustration in the cubic spinels MAl_2O_4 ($M=Co, Fe, \text{ and } Mn$), Phys. Rev. B **72**, 174404 (2005).
- [5] G. Chen, L. Balents, and A. P. Schnyder, Spin-Orbital Singlet and Quantum Critical Point on the Diamond Lattice: FeSc₂S₄, Phys. Rev. Lett. **102**, 096406 (2009).

- [6] O. Zaharko, N. B. Christensen, A. Cervellino, V. Tsurkan, A. Maljuk, U. Stuhr, C. Niedermayer, F. Yokaichiya, D. N. Argyriou, M. Boehm, and A. Loidl, Spin liquid in a single crystal of the frustrated diamond lattice antiferromagnet CoAl_2O_4 , *Phys. Rev. B* **84**, 094403 (2011).
- [7] L. Ge, J. Flynn, J. A. M. Paddison, M. B. Stone, S. Calder, M. A. Subramanian, A. P. Ramirez, and M. Mourigal, Spin order and dynamics in the diamond-lattice Heisenberg antiferromagnets CuRh_2O_4 and CoRh_2O_4 , *Phys. Rev. B* **96**, 064413 (2017).
- [8] G. J. MacDougall, D. Gout, J. L. Zarestky, G. Ehlers, A. Podlesnyak, and M. A. Mcguire, Kinetically inhibited order in a diamond-lattice antiferromagnet, *Proc. Natl. Acad. Sci. U. S. A.* **108**, 15693 (2011).
- [9] D. Bergman, J. Alicea, E. Gull, S. Trebst, and L. Balents, Order-by-disorder and spiral spin-liquid in frustrated diamond-lattice antiferromagnets, *Nat. Phys.* **3**, 487 (2007).
- [10] S. Gao, O. Zaharko, V. Tsurkan, Y. Su, J. S. White, G. S. Tucker, B. Roessli, F. Bourdarot, R. Sibille, D. Chernyshov, T. Fennell, A. Loidl, and C. Rüegg, Spiral spin-liquid and the emergence of a vortex-like state in MnSc_2S_4 , *Nat. Phys.* **13**, 157 (2017).
- [11] C. Wang, A. Nahum, and T. Senthil, Topological paramagnetism in frustrated spin-1 Mott insulators, *Phys. Rev. B* **91**, 195131 (2015).
- [12] G. Chen, Quantum paramagnet and frustrated quantum criticality in a spin-one diamond lattice antiferromagnet, *Phys. Rev. B* **96**, 020412(R) (2017).
- [13] J. R. Chamorro, L. Ge, J. Flynn, M. A. Subramanian, M. Mourigal, and T. M. McQueen, Frustrated spin one on a diamond lattice in NiRh_2O_4 , *Phys. Rev. Mater.* **2**, 034404 (2018).
- [14] K. A. Modic, T. E. Smidt, I. Kimchi, N. P. Breznay, A. Biffin, S. Choi, R. D. Johnson, R. Coldea, P. Watkins-Curry, G. T. McCandless, J. Y. Chan, F. Gandara, Z. Islam, A. Vishwanath, A. Shekhter, R. D. McDonald, and J. G. Analytis, Realization of a three-dimensional spin-anisotropic harmonic honeycomb iridate, *Nat. Commun.* **5**, 4203 (2014).
- [15] I. Kimchi, J. G. Analytis, and A. Vishwanath, Three-dimensional quantum spin liquids in models of harmonic-honeycomb iridates and phase diagram in an infinite- D approximation, *Phys. Rev. B* **90**, 205126 (2014).
- [16] M. M. Bordelon, C. Liu, L. Posthuma, E. Kenney, M. J. Graf, N. P. Butch, A. Banerjee, S. Calder, L. Balents, and S. D. Wilson, Frustrated Heisenberg $J_1 - J_2$ model within the stretched diamond lattice of LiYbO_2 , *Phys. Rev. B* **103**, 014420 (2021).
- [17] M. M. Bordelon, J. D. Bocarsly, L. Posthuma, A. Banerjee, Q. Zhang, and S. D. Wilson, Antiferromagnetism and crystalline-electric field excitations in tetragonal NaCeO_2 , *Phys. Rev. B* **103**, 024430 (2021).
- [18] A. Hristea, E. J. Popovici, L. Muresan, M. Stefan, R. Grecu, A. Johansson, and M. Boman, Morphostructural and luminescent investigations of niobium activated yttrium tantalate powders, *J. Alloys Compd.* **471**, 524 (2009).
- [19] O. Voloshyna, S. V. Neicheva, N. G. Starzhinskiy, I. M. Zenya, S. S. Gridin, V. N. Baumer, and O. T. Sidletskiy, Luminescent and scintillation properties of orthotantalates with common formulae RETaO_4 ($\text{RE} = \text{Y}, \text{Sc}, \text{La}, \text{Lu}$ and Gd), *Mater. Sci. Eng. B Solid-State Mater. Adv. Technol.* **178**, 1491 (2013).
- [20] R. Haugrud and T. Norby, Proton conduction in rare-earth ortho-niobates and ortho-tantalates, *Nat. Mater.* **5**, 193 (2006).
- [21] C. Li, R. D. Bayliss, and S. J. Skinner, Crystal structure and potential interstitial oxide ion conductivity of LnNbO_4 and $\text{LnNb}_{0.92}\text{W}_{0.08}\text{O}_{4.04}$ ($\text{Ln} = \text{La}, \text{Pr}, \text{Nd}$), *Solid State Ionics* **262**, 530 (2014).
- [22] D. W. Kim, D. K. Kwon, S. H. Yoon, and K. S. Hong, Microwave dielectric properties of rare-earth ortho-niobates with ferroelasticity, *J. Am. Ceram. Soc.* **89**, 3861 (2006).
- [23] J. Wang, X. Y. Chong, R. Zhou, and J. Feng, Microstructure and thermal properties of RETaO_4 ($\text{RE} = \text{Nd}, \text{Eu}, \text{Gd}, \text{Dy}, \text{Er}, \text{Yb}, \text{Lu}$) as promising thermal barrier coating materials, *Scr. Mater.* **126**, 24 (2017).
- [24] A. I. Komkov, The Structure of Natural Fergusonite, and of a Polymorphic Modification, *Kristallografiya* **4**, 836 (1959).
- [25] C. Keller, Über ternäre Oxide des Niobs und Tantalums vom Typ ABO_4 , *Zeitschrift für Anorg. und Allg. Chemie* **318**, 89 (1962).
- [26] H. P. Rooksby and E. A. D. White, The structures of 1:1 compounds of rare earth oxides with niobia and tantalum, *Acta Crystallogr.* **16**, 888 (1963).
- [27] G. M. Wolten, The structure of the M' -phase of YTaO_4 , a third Fergusonite polymorph, *Acta Crystallogr.* **23**, 939 (1967).
- [28] L. H. Brixner and H. Y. Chen, On the Structural and Luminescent Properties of the M' LnTaO_4 Rare Earth Tantalates, *J. Electrochem. Soc.* **130**, 2435 (1983).
- [29] S. A. Mather and P. K. Davies, Nonequilibrium Phase Formation in Oxides Prepared at Low Temperature: Fergusonite-Related Phases, *J. Am. Ceram. Soc.* **78**, 2737 (1995).
- [30] M. A. Ryumin, E. G. Sazonov, V. N. Guskov, P. G. Gagarin, A. V. Khoroshilov, A. V. Guskov, K. S. Gavrichev, L. K. Baldaev, I. V. Mazilin, and L. N. Golushina, Thermodynamic properties of GdTaO_4 , *Inorg. Mater.* **53**, 728 (2017).
- [31] M. Saura-Múzquiz, B. G. Mullens, H. E. Maynard-Casely, and B. J. Kennedy, Neutron diffraction study of the monoclinic-tetragonal phase transition in NdNbO_4 and NdTaO_4 , *Dalt. Trans.* **50**, 11485 (2021).
- [32] V. S. Stubičan, High-Temperature Transitions in Rare-Earth Niobates and Tantalates, *J. Am. Ceram. Soc.* **47**, 55 (1964).
- [33] I. Hartenbach, F. Lissner, T. Nikelski, S. F. Meier, H. Müller-Bunz, and T. Schleid, Über oxotantalate der lanthanide des formeltyps MTaO_4 ($\text{M} = \text{La} - \text{Nd}, \text{Sm} - \text{Lu}$), *Zeitschrift für Anorg. und Allg. Chemie* **631**, 2377 (2005).
- [34] A. Santoro, M. Marezio, R. S. Roth, and D. Minor, Neutron powder diffraction study of the structures of CeTaO_4 , CeNbO_4 , and NdTaO_4 , *J. Solid State Chem.* **35**, 167 (1980).
- [35] S. Tsunekawa, T. Kamiyama, K. Sasaki, H. Asano, and T. Fukuda, Precise structure analysis by neutron diffraction for RNbO_4 and distortion of NbO_4 tetrahedra, *Acta Crystallogr. Sect. A* **49**, 595 (1993).
- [36] P. Sarin, R. W. Hughes, D. R. Lowry, Z. D. Apostolov, and W. M. Kriven, High-temperature properties and ferroelastic phase transitions in rare-earth niobates (LnNbO_4), *J. Am. Ceram. Soc.* **97**, 3307 (2014).

- [37] F. F. Y. Wang and R. L. Gravel, Magnetic and Electrical Properties of NdNbO_4 and GdNbO_4 , *Phys. Status Solidi* **12**, 609 (1965).
- [38] J. D. Cashion, A. H. Cooke, M. J. M. Leask, T. L. Thorp, and M. R. Wells, Crystal growth and magnetic susceptibility of some rare-earth compounds - Part 2 Magnetic Susceptibility Measurements on a Number of Rare-Earth Compounds, *J. Mater. Sci.* **3**, 402 (1968).
- [39] A. T. Starovoitov, V. I. Ozhogin, and V. A. Bokov, The Study of the Magnetic Properties of Several Rare-Earth Niobates in Strong Pulsed Fields, *Phys. Status Solidi* **32**, 151 (1969).
- [40] S. Tsunekawa, H. Yamauchi, Y. Yamaguchi, and T. Fukuda, Paramagnetic properties of ferroelastic rare earth orthoniobates, *J. Alloys Compd.* **192**, 108 (1993).
- [41] S. Tsunekawa, H. Yamauchi, K. Sasaki, Y. Yamaguchi, and T. Fukuda, Paramagnetic anisotropies in RTaO_4 ($R = \text{Nd, Ho and Er}$) crystals, *J. Alloys Compd.* **245**, 89 (1996).
- [42] R. J. Cava and R. S. Roth, The structure of LaTaO_4 at 300°C by neutron powder profile analysis, *J. Solid State Chem.* **36**, 139 (1981).
- [43] H. M. Rietveld, A profile refinement method for nuclear and magnetic structures, *J. Appl. Crystallogr.* **2**, 65 (1969).
- [44] A. A. Coelho, TOPAS and TOPAS-Academic: An optimization program integrating computer algebra and crystallographic objects written in C++, *J. Appl. Crystallogr.* **51**, 210 (2018).
- [45] R. A. Young, ed., *The Rietveld Method* (Oxford University Press, 1993).
- [46] K. Momma and F. Izumi, VESTA 3 for three-dimensional visualization of crystal, volumetric and morphology data, *J. Appl. Crystallogr.* **44**, 1272 (2011), arXiv:arXiv:1011.1669v3.
- [47] J. Rodríguez-Carvajal, Recent advances in magnetic structure determination by neutron powder diffraction, *Phys. B* **192**, 55 (1993).
- [48] D. Smith and F. Fickett, Low-Temperature Properties of Silver, *J. Res. Natl. Inst. Stand. Technol.* **100**, 119 (1995).
- [49] E. S. R. Gopal, *Specif. Heats Low Temp.* (Springer US, Boston, MA, 1966).
- [50] V. Y. Markiv, N. M. Belyavina, M. V. Markiv, Y. Titov, A. M. Sych, A. N. Sokolov, A. A. Kapshuk, and M. S. Slobodyanyk, Peculiarities of polymorphic transformations in YbTaO_4 and crystal structure of its modifications, *J. Alloys Compd.* **346**, 263 (2002).
- [51] P. Wu, Y. Zhou, F. Wu, M. Hu, X. Chong, and J. Feng, Theoretical and experimental investigations of mechanical properties for polymorphous YTaO_4 ceramics, *J. Am. Ceram. Soc.* **102**, 7656 (2019).
- [52] P. Wu, X. Chong, F. Wu, M. Hu, H. Guo, and J. Feng, Investigation of the thermophysical properties of $(\text{Y}_{1-x}\text{Yb}_x)\text{TaO}_4$ ceramics, *J. Eur. Ceram. Soc.* **40**, 3111 (2020).
- [53] R. D. Shannon, Revised Effective Ionic Radii and Systematic Studies of Interatomic Distances in Halides and Chalcogenides, *Acta Crystallogr.* **A32**, 751 (1976).
- [54] N. D. Kelly, C. V. Colin, S. E. Dutton, V. Nassif, I. Puente Orench, and E. Suard, Nuclear and magnetic diffraction study of monoclinic TbTaO_4 , *Inst. Laue-Langevin* 10.5291/ILL-DATA.5-31-2854 (2021).
- [55] M. B. Sanders, F. A. Cevallos, and R. J. Cava, Magnetism in the $\text{KBaRE}(\text{BO}_3)_2$ ($\text{RE} = \text{Sm, Eu, Gd, Tb, Dy, Ho, Er, Tm, Yb, Lu}$) series: Materials with a triangular rare earth lattice, *Mater. Res. Express* **4**, 036102 (2017).
- [56] S. Guo, T. Kong, W. Xie, L. Nguyen, K. Stolze, F. A. Cevallos, and R. J. Cava, Triangular Rare-Earth Lattice Materials $\text{RbBaR}(\text{BO}_3)_2$ ($R = \text{Y, Gd-Yb}$) and Comparison to the $\text{KBaR}(\text{BO}_3)_2$ Analogs, *Inorg. Chem.* **58**, 3308 (2019).
- [57] H. Nishimine, M. Wakeshima, and Y. Hinatsu, Structures, magnetic, and thermal properties of Ln_3MoO_7 ($\text{Ln} = \text{La, Pr, Nd, Sm, and Eu}$), *J. Solid State Chem.* **178**, 1221 (2005).
- [58] B. Vijaya Kumar, R. Velchuri, V. Rama Devi, B. Sreedhar, G. Prasad, D. Jaya Prakash, M. Kanagaraj, S. Arumugam, and M. Vithal, Preparation, characterization, magnetic susceptibility (Eu, Gd and Sm) and XPS studies of $\text{Ln}_2\text{ZrTiO}_7$ ($\text{Ln} = \text{La, Eu, Dy and Gd}$), *J. Solid State Chem.* **184**, 264 (2011).
- [59] M. B. Sanders, J. W. Krizan, and R. J. Cava, $\text{RE}_3\text{Sb}_3\text{Zn}_2\text{O}_{14}$ ($\text{RE} = \text{La, Pr, Nd, Sm, Eu, Gd}$): A new family of pyrochlore derivatives with rare earth ions on a 2D Kagome lattice, *J. Mater. Chem. C* **4**, 541 (2016).
- [60] S. T. Bramwell, M. N. Field, M. J. Harris, and I. P. Parkin, Bulk magnetization of the heavy rare earth titanate pyrochlores - A series of model frustrated magnets, *J. Phys. Condens. Matter* **12**, 483 (2000).
- [61] R. J. C. Dixey and P. J. Saines, Optimization of the Magnetocaloric Effect in Low Applied Magnetic Fields in LnOHCO_3 Frameworks, *Inorg. Chem.* **57**, 12543 (2018).
- [62] M. E. Fisher, Relation between the specific heat and susceptibility of an antiferromagnet, *Philos. Mag.* **7**, 1731 (1962).
- [63] A. P. Ramirez, Strongly geometrically frustrated magnets, *Annu. Rev. Mater. Sci.* **24**, 453 (1994).
- [64] P. Mukherjee, A. C. Sackville Hamilton, H. F. J. Glass, and S. E. Dutton, Sensitivity of magnetic properties to chemical pressure in lanthanide garnets $\text{Ln}_3\text{A}_2\text{X}_3\text{O}_{12}$, $\text{Ln} = \text{Gd, Tb, Dy, Ho}$, $\text{A} = \text{Ga, Sc, In, Te}$, $\text{X} = \text{Ga, Al, Li}$, *J. Phys. Condens. Matter* **29**, 405808 (2017).
- [65] Y. Hashimoto, M. Wakeshima, and Y. Hinatsu, Magnetic properties of ternary sodium oxides NaLnO_2 ($\text{Ln} = \text{rare earths}$), *J. Solid State Chem.* **176**, 266 (2003).
- [66] G. Sala, M. B. Stone, B. K. Rai, A. F. May, D. S. Parker, G. B. Halász, Y. Q. Cheng, G. Ehlers, V. O. Garlea, Q. Zhang, M. D. Lumsden, and A. D. Christianson, Crystal field splitting, local anisotropy, and low-energy excitations in the quantum magnet YbCl_3 , *Phys. Rev. B* **100**, 180406(R) (2019).
- [67] H. Cho, R. Nirmala, J. Jeong, P. J. Baker, H. Takeda, N. Mera, S. J. Blundell, M. Takigawa, D. T. Adroja, and J.-G. Park, Dynamic spin fluctuations in the frustrated A-site spinel CuAl_2O_4 , *Phys. Rev. B* **102**, 014439 (2020).
- [68] V. Fritsch, J. Hemberger, N. Büttgen, E. W. Scheidt, H. A. Krug Von Nidda, A. Loidl, and V. Tsurkan, Spin and Orbital Frustration in MnSc_2S_4 and FeSc_2S_4 , *Phys. Rev. Lett.* **92**, 116401 (2004).
- [69] V. K. Trunov and L. N. Kinzhibalo, Change of LnNbO_4 structures in lanthanoid series, *Dokl. Akad. Nauk SSSR* **263**, 348 (1982).
- [70] P. Mukherjee, E. Suard, and S. E. Dutton, Magnetic properties of monoclinic lanthanide metaborates, $\text{Ln}(\text{BO}_2)_3$, $\text{Ln} = \text{Pr, Nd, Gd, Tb}$, *J. Phys. Condens. Matter* **29**, 405807 (2017).

- [71] G. W. Howieson, S. Wu, A. S. Gibbs, W. Zhou, J. F. Scott, and F. D. Morrison, Incommensurate–Commensurate Transition in the Geometric Ferroelectric LaTaO_4 , *Adv. Funct. Mater.* **30**, 1 (2020).
- [72] G. W. Howieson, K. K. Mishra, A. S. Gibbs, R. S. Katiyar, J. F. Scott, F. D. Morrison, and M. Carpenter, Structural phase transitions in the geometric ferroelectric LaTaO_4 , *Phys. Rev. B* **103**, 014119 (2021).
- [73] A. Dias, K. P. F. Siqueira, and R. L. Moreira, Micro far-infrared dielectric response of lanthanide orthotantalates for applications in microwave circuitry, *J. Alloys Compd.* **693**, 1243 (2017).